



Effect Temperature for improving the Li-ion conductivity of $\text{Li}_7\text{La}_3\text{Zr}_2\text{O}_{12}$

Agnes Lakshmanan ^a, Sabarinathan Venkatachalam ^{a, b, *}

^a Department of Physics, Manonmaniam Sundaranar University, Tirunelveli-627012, Tamil Nadu, India

^b Department of Renewable Energy Science, Manonmaniam Sundaranar University, Tirunelveli-627012, Tamil Nadu, India.

*Corresponding Author Email: sabarinathan.msu@gmail.com

DOI: <https://doi.org/10.54392/irjmt2417>

Received: 13-10-2023; Revised: 24-12-2023; Accepted: 28-12-2023; Published: 26-01-2024



Abstract: This study investigates the dissociation behavior of water-soluble salts of Li and La and the unique behavior of Zr sources, resulting in the generation of Li^+ , La^{3+} , and Zr^{4+} ions in aqueous solutions. The specific conductivity of calcined SG1 and SG2 displays temperature-dependent variations, with SG1 consistently exhibiting higher conductivity (2.08×10^{-4} S/cm) across the temperature range. The closed-packed structure facilitates the controllable mass transfer of lithium, enhancing ionic conductivity. The constructed $\text{LiFePO}_4/\text{LLZO}/\text{AC}$ device using these electrolytes demonstrates an impressive energy density of 1.95 Wh/kg and a power density of 144.92 W/kg, showcasing an excellent solid electrode-electrolyte interphase. Over 10,000 cycles, cyclic stability, with an average performance of 86%, underscores the potential of LLZO as a solid electrolyte for advanced energy storage devices. The sol-gel synthesis and densification strategy is a simple and effective method for obtaining lithium-rich LLZO electrolytes. The enhanced ionic conductivity and electrochemical performance of the solid-state device emphasize the practical viability of this approach, contributing to the sustainable development of advanced energy storage technologies.

Keywords: LLZO, Garnet type-electrolytes, Ionic conductivity, Solid device

1. Introduction

Renewable energy sources, such as wind or solar photovoltaic, are poised to revolutionize the energy industry and usher in a sustainable future. The shift from conventional carbon-based fossil fuels to electricity derived from sustainable sources necessitates an effective form of energy storage characterized by high energy and power capacities. In this context, Lithium-based systems have garnered significant attention, particularly for their application in portable electronic devices due to their impressive power and energy density [1]. Li-ion batteries (LIBs) play a pivotal role in advancing emerging applications such as electric vehicles and large-scale energy storage. Despite their widespread use and established reliability, the current electrolytes utilized in LIBs, whether organic solvents or polymers with dissolved Li-salt, impose limitations on their applications. Due to their flammability and volatility, traditional organic liquid electrolytes raise safety concerns for battery systems. The achievable energy density of LIBs is constrained by the inadequate electrochemical stability of these organic components, limiting the selection of electrode materials.

To address these challenges, there is a growing interest in replacing organic liquid electrolytes with more

stable inorganic solid ion conductors [2]. The development of solid-state electrolytes (SSEs) is gaining momentum, driven by the potential advantages of being non-flammable and stable when in contact with the lithium metal anode [3]. A key characteristic sought in these materials is a combination of high ionic conductivity, low electronic conductivity, and robust stability against both anode and cathode reactions, particularly when operating at room temperature. Furthermore, electrolyte materials employed in Li-ion batteries (LIBs) can be polymeric or ceramic. Polymer solid electrolytes consist of a polymer host with a dissolved salt, offering improved interfaces through specific processing. However, their application at room temperature is constrained by their relatively low ionic conductivity.

In contrast, despite exhibiting lower ionic conductivity compared to polymers, ceramics have garnered significant attention for their high-temperature reliability among electrolyte materials. Various ceramic electrolytes with ionic conductivity comparable to liquid electrolytes have been explored for Solid-State Lithium-Ion Batteries (SSLIBs). These ceramics include sulfide-type glasses [4, 5], NASICON-type phosphates [6, 7], perovskite-type titanates [8, 9], and garnet-type oxides, encompassing both sulfides and oxides.

Among oxides, NASICON-type electrolytes stand out for their stability in air and water and high lithium-ion conductivity, enabling charge carrier migration in all three dimensions. A representative NASICON-type electrolyte, $\text{Li}_{1.3}\text{Al}_{0.3}\text{Ti}_{1.7}(\text{PO}_4)_3$, possesses a skeleton conducive to ionic migration, displaying notable ionic conductivity at 25°C, reaching 7×10^{-4} S/cm. Despite these advantages, NASICON-type electrolytes face challenges such as poor interfacial contact and instability with Li metal, attributed to the facile reduction of Ti^{4+} . Similarly, perovskite-type electrolytes share drawbacks with NASICON-type, achieving grain conductivity close to 10^{-3} S/cm but facing relatively low total conductivity due to high boundary resistance [10]. Conversely, sulfide materials exhibit high ionic conductivity, potentially attributed to the polarizable sulfide ion. However, sulfide materials present challenges as they are hygroscopic and can produce toxic H_2S gas when moistened, reacting adversely with O_2 and impacting research applications. On the other hand, oxides are generally chemically stable and easy to handle. Nevertheless, they present critical issues related to toughness, brittleness, and significant grain boundary resistance due to unstable contact between solids and electrodes [10].

The garnet-type material $\text{Li}_7\text{La}_3\text{Zr}_2\text{O}_{12}$, renowned for its Li-ion conductivity, is considered a highly promising Solid-State Electrolyte (SSE). It stands out due to its elevated ionic conductivity, favorable electrochemical window, chemical stability against lithium metal, and low hygroscopic properties. The garnet-type $\text{La}_3\text{Li}_5\text{M}_2\text{O}_{12}$ ($\text{M} = \text{Nb}, \text{Ta}$) was initially described by Mazza [11] and Hyooma [12] in 1988, with the ionic mobility in $\text{La}_3\text{Li}_5\text{M}_2\text{O}_{12}$ crystalline first reported by Thangadurai et al. in 2003 [13].

Another variant, the $\text{Li}_7\text{La}_3\text{Zr}_2\text{O}_{12}$ -type material, introduced by Murugan et al. in 2007 [14], is a promising SSE achieved through aliovalent substitution at room temperature. Through the substitution of Zr on Nb and Ta, the ceramic material $\text{Li}_7\text{La}_3\text{Zr}_2\text{O}_{12}$ (LLZO) exhibited remarkable Li^+ conductivity (3×10^{-4} Scm^{-1} at 25°C), making it a compelling candidate as a solid-state Li-ion conductor. Subsequently, Awaka et al. in 2009 [15] discovered a distorted version of the tetragonal phase (t-LLZO, I41/acd) with lower conductivity than the cubic phase (c-LLZO, Ia $\bar{3}$ d), and this distortion appears to be thermally stable.

All garnets reported thus far with 7 Li per formula unit ($\text{Li}_7\text{Ln}_3\text{M}_2\text{O}_{12}$, where $\text{Ln} = \text{La}, \text{Nd}$; $\text{M} = \text{Sn}, \text{Hf}, \text{Zr}$) exhibit tetragonal symmetry. The $\text{Li}_7\text{La}_3\text{Zr}_2\text{O}_{12}$ material adopts a tetragonal cell due to its high Li content, favouring long $\text{Li}^+ - \text{Li}^+$ interactions. Generally, the tetragonal phase tends to have lower conductivity than the cubic phase. However, the cubic phase is unstable and easily transforms into a tetragonal structure during sintering [16]. When a tetragonal to cubic transition

occurs, there is a shift from sites 8a to 16e, both subsets of 24d.

In this context, LLZO powders were synthesized using two sol-gel methods, employing citric acid as a chelating agent and ethylene glycol as an organic solvent. These methods are known as the Citric-Nitrates route and the Citric-Oxide route. In the Citric-Nitrates and Citric-Oxide routes, water-soluble salts of Li and La undergo dissociation, providing single valence Li^+ and La^{3+} ions within the solution. However, the dissociation behavior differs for water-soluble Zr sources, where ZrOCl_2 produces Zr^{4+} ions in aqueous solutions. The effect of annealing on Li-ion mobility was examined systematically using X-ray diffraction and Raman spectroscopy. The structural morphology of the LLZO pellet was studied using atomic force and scanning electron microscopy. The compositional dependency of electrical conductivities and relaxation properties was investigated using a symmetrical cell of pelletized LLZO. The relaxation property of composite materials was investigated using the dielectric module formalism, yielding new insights into electrical conductivity and material relaxation. The ionic conductivity ranged from 10^{-5} to 10^{-3} S/cm, depending on the synthesis and sintering conditions, with sintering improving electrochemical characteristics throughout a wide range. Additionally, the electrochemical performance of the $\text{LiFePO}_4/\text{LLZO}/\text{AC}$ device with liquid electrolyte encapsulation was assessed, taking into account the rate capacity and cycle performance.

2. Experimental

LLZO (Lithium Lanthanum Zirconium Oxide) ceramic powders were produced via two sol-gel methods, namely SG1 and SG2. The chemicals used in the synthesis were obtained from Alfa Aesar and used directly without further treatments. The molecular ratio of Li: La: Zr is 7:3:4, while the molar ratios of organic and complexing agents were 20:30, respectively.

2.1 Preparation

The first sol-gel method, SG1, was synthesized using the citrate-nitrate route. The precursor materials used for the nitrate-sol preparation were Lithium Nitrate (LiNO_3), Lanthanum Nitrate ($\text{La}(\text{NO}_3)_3 \cdot 6\text{H}_2\text{O}$), and Zirconyl Chloride ($\text{ZrOCl}_2 \cdot 8\text{H}_2\text{O}$). The stoichiometric amounts of these precursor powders were dissolved in 20 ml of deionized water under moderate stirring for 24 hrs, as depicted in Figure 1(a). Highly concentrated citric acid ($\text{C}_6\text{H}_8\text{O}_7$) and ethylene glycol ($\text{C}_2\text{H}_6\text{O}_2$) were added as organic and complexing agents. The added solutions were stirred continuously for 3 hrs at 333 K to form a homogeneous sol [17]. Subsequently, the precursor was decomposed at 373 K for 6 hrs to dry. The dried gel was then pulverized and pyrolyzed at 873 K for 6 hrs to produce the LLZO polycrystalline phase. The obtained

powders were crushed and pelletized using an 8mm axial press with 5 tons of pressure. Calcination was carried out in an alumina crucible at 1323 K for 12 hrs to obtain the final LLZO powder.

The second sol-gel method, SG2, was synthesized using the oxide-nitrate route. The oxide sols were prepared using the powders of Lithium Carbonate (Li_2CO_3), Lanthanum Oxide (La_2O_3), Zirconyl Chloride ($\text{ZrOCl}_2 \cdot 8\text{H}_2\text{O}$), and Nitric acid (HNO_3). Dilute HNO_3 was used to dissolve Li_2CO_3 and La_2O_3 , which were continuously stirred at 333 K for 1 hr, as dissipated in Figure 1(b). Simultaneously, $\text{ZrOCl}_2 \cdot 8\text{H}_2\text{O}$ was dissolved in deionized water. The two solutions were subsequently combined and mixed until a homogeneous solution was achieved [18]. For the synthesis of the sol, high concentrations of $\text{C}_6\text{H}_8\text{O}_7$ and $\text{C}_2\text{H}_6\text{O}_2$ were used as organic and complexing agents. The solutions were continuously stirred for 3 hrs at 333 K to form a homogeneous sol. The resulting precursor was dried and decomposed at 373 K for 6 hrs. The dried gel was pulverized and pyrolyzed for 6 hrs at 873 K to obtain the LLZO polycrystalline phase. The resulting powders were crushed and pelletized using an 8mm axial press under a 5-ton pressure. The calcination was carried out in an alumina crucible at 1323 K for 12 hours to produce the final LLZO powder. During the calcination process, the pellet was covered with mother powder bed to minimize the risk of unexpected Li^+ loss. This protective measure was taken to ensure the integrity and stability of the final product.

2.2 Characterization

The crystal structure of $\text{Li}_7\text{La}_3\text{Zr}_2\text{O}_{12}$ was examined by X-ray diffraction (XRD) research on a

PANalytical instrument X' Pert Pro Diffractometer, with $\text{Cu K}\alpha 1$ radiation in the 2θ range of 10° – 80° . The phase identification was carried out by comparing the resulting diffraction pattern to the joint committee on powder diffraction standards (JCPDS) database. In addition, confocal Raman imaging was performed with the WITec alpha-300R instrument, which used a 632 nm laser. The microstructure of $\text{Li}_7\text{La}_3\text{Zr}_2\text{O}_{12}$ was examined using scanning electron microscopy (SEM) on the Carl ZEISS - EVO 10 instrument. Furthermore, the surface morphology was examined with an atomic force microscope (AFM) from Oxford Instruments, specifically the MFD-3D Origin.

Electrochemical impedance spectroscopy (EIS) measurements were performed using Bio-Logic Science Instruments (VSP-300) at temperatures ranging from 323K to 723K. The frequency range for the EIS experiments was 7MHz to 100mHz, with an amplitude of 25mV. The pelletized LLZO, shown in Figure 1, was polished to a uniform thickness of 1mm and sputtered with Ag as Li-blocking electrodes ($\text{Ag} \parallel \text{LLZO} \parallel \text{Ag}$) for EIS measurements. Following characterization, the pelletized LLZO was used to fabricate the device.

2.3 Fabrication of $\text{LiFePO}_4/\text{LLZO}/\text{AC}$ device

The $\text{LiFePO}_4/\text{LLZO}/\text{AC}$ device was built utilizing the CR2032 configuration at 303 K. In this configuration, the cathode and anode were lithium iron phosphate (LFP) and activated carbon (AC). The composed solid-state electrochemical device was prepared using the method described by Agnes et al [19].

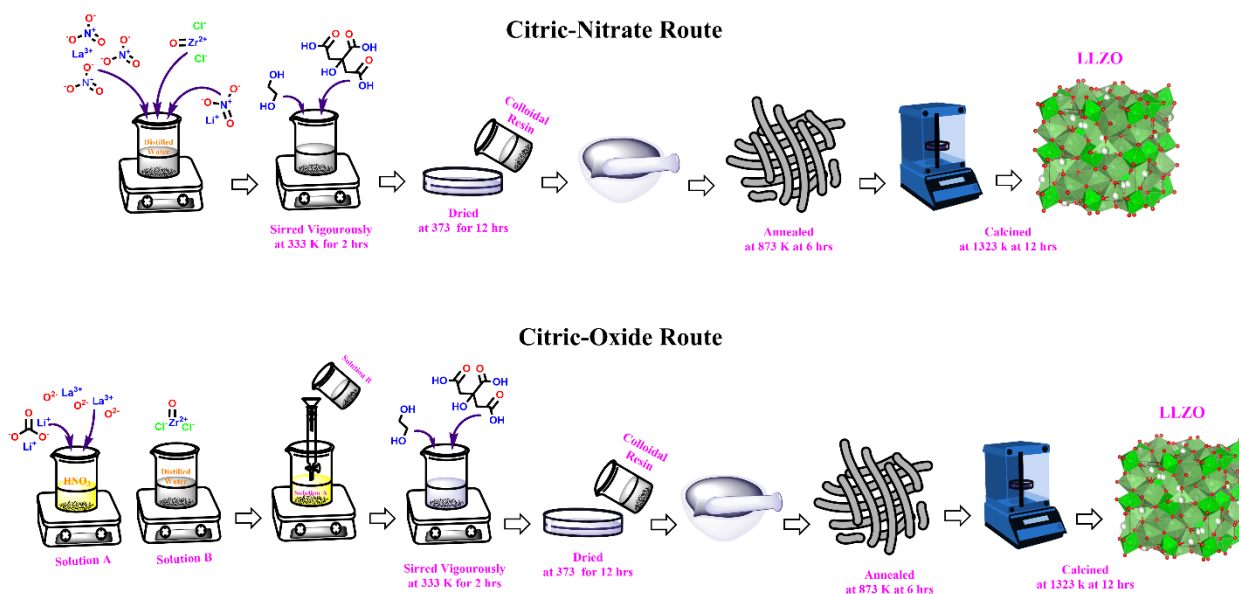


Figure 1. Process flow chart describing the sol-gel synthesis of $\text{Li}_7\text{La}_3\text{Zr}_2\text{O}_{12}$

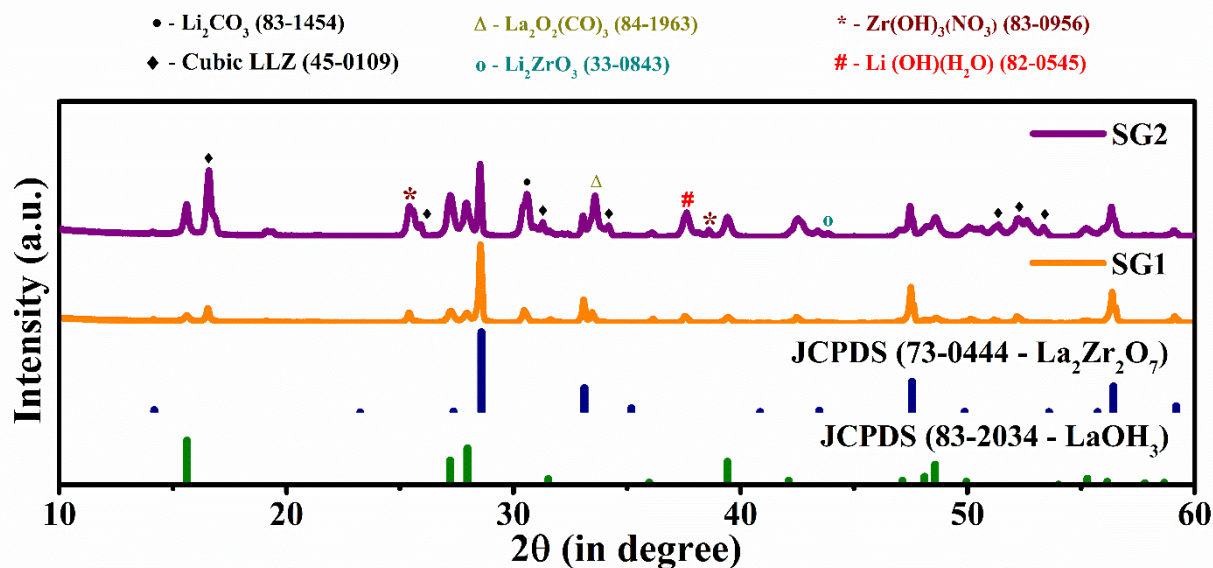


Figure 2. X-ray Diffraction patterns of LLZO powder prepared by Sol-Gel process calcined at 1323K for 12h.

3. Results and Discussion

3.1 XRD analysis

Figure 2 displays the X-ray diffraction patterns of LLZO samples SG1 and SG2, which were synthesized using the Sol-gel process. The diffraction patterns of SG1 and SG2, after being calcined at 1323K, reveal the presence of tetragonal distortion within the cubic lattice, along with some additional phases. The diffraction peaks were identified using the Joint Committee of Powder Diffraction Standard (JCPDS) card no. 73-0444, which corresponds to $\text{La}_2\text{Zr}_2\text{O}_7$, along with several other phases, such as LaOH_3 (PDF # 83-2034), Cubic LLZO (PDF # 45-0109, represented by symbol \blacklozenge), Li_2CO_3 (PDF # 83-1454, represented by symbol \bullet), $\text{La}_2\text{O}_2(\text{CO}_3)$ (PDF # 84-1963, represented by symbol Δ), Li_2ZrO_3 (PDF # 33-0843, represented by symbol \circ), $\text{Li}(\text{OH})(\text{H}_2\text{O})$ (PDF # 82-0545, represented by symbol $\#$), and $\text{Zr}(\text{OH})_3(\text{NO}_3)$ (PDF # 83-0956, represented by symbol $*$). [20]

The presence of secondary phases can be attributed to significant lithium loss in the material. Among these, JCPDS card no. 73-0444 ($\text{La}_2\text{Zr}_2\text{O}_7$) is recognized as a standard byproduct of LLZO and is observed in higher abundance compared to the cubic LLZO phase. The loss of lithium due to evaporation at elevated temperatures can contribute to this transformation. When lithium evaporates from the structure, it can disrupt the LLZO lattice and favor the formation of $\text{La}_2\text{Zr}_2\text{O}_7$ [21]. It's important to note that pure precursor powders alone cannot form cubic phases when exposed to air conditions. Additionally, the diffraction peak of SG2 displays a splitting of peaks, which corresponds to the tetragonal phase of LLZO. Notably, the prepared samples were synthesized at

stoichiometric ratios of elements without the addition of excess Li^+ . However, lithium concentration in the samples decreases due to reactions with CO_2 and H_2O present in the air.

In Figure 2, it's evident that SG-1 produces more favourable results when compared to SG-2. SG-1 not only indicates the formation of standard LLZO but also reveals the presence of faint secondary phases, which indicate significant lithium loss. These secondary phases include LaOH_3 , $\text{La}_2\text{O}_2(\text{CO}_3)$, $\text{Li}(\text{OH})(\text{H}_2\text{O})$, Li_2ZrO_3 , and $\text{Zr}(\text{OH})_3(\text{NO}_3)$. This observation suggests that including $(\text{NO}_3)^-$ ions hampers the formation and transformation of the cubic phase from the tetragonal phase. The presence of nitrate ions appears to hinder the stabilization of the cubic LLZO phase in SG-1 [17]. Conversely, the diffraction patterns in SG-2 appear relatively weak, with the most prominent peaks associated with $\text{La}_2\text{Zr}_2\text{O}_7$. This may be attributed to the inadequate mixing of the precursor solution, which results in side reactions leading to the formation of $\text{La}_2\text{Zr}_2\text{O}_7$. The diffraction patterns in SG-2 also show some major secondary reflections, which could be attributed to residual lithium carbonate. In certain high-angle reflections, bifurcations (peak doublets) suggests a tetragonal distortion of the cubic lattice in LLZO [22, 23].

It's crucial to emphasize that the peak splitting observed in SG-2 is not present in SG-1, indicating a mixture of cubic and tetragonal phases in SG-2. In contrast, the diffraction peaks in SG-1 are narrow and sharp and lack characteristic peaks of the tetragonal phase. This strongly suggests that LLZO primarily exists in a pure cubic phase in SG-1. Additionally, the grain size of the particles was determined using the Debye-

Scherrer formula. Based on the highest intensity peak (2 2 2), the average grain sizes of SG1 and SG2 were calculated to be 7 nm and 13 nm, respectively. Consequently, further analyses were conducted on the SG-1 sample due to its superior performance and larger calculated grain size than SG-2.

3.2 Raman Analysis

Figure 3 shows the Raman spectra of LLZO samples SG1 and SG2, which exhibit vibrational modes associated with the phase transition from cubic LLZO (c-LLZO) to tetragonal LLZO (t-LLZO), which is consistent with XRD findings. Raman spectra can be divided into three categories: low-energy below 300 cm^{-1} , intermediate-energy between 300 and 550 cm^{-1} , and high-energy over 550 cm^{-1} . The high-frequency spectra show vibrational stretching modes of ZrO_6 octahedral units. The intermediate region is predominantly made up of vibrational bending modes of both octahedral (LiO_6) and tetrahedral units (LiO_4). Finally, the low-frequency zone corresponds to translational modes associated with the movement of mobile cations, which is related to the vibration of heavy La cations in the structure. This categorization of Raman spectra aids in the detailed analysis of the material's vibrational characteristics [24].

The Raman spectra of SG1 exhibit distinct peaks at 141, 177, 240, 263, 343, 782, 893, 981, and 1026 cm^{-1} , which are attributed to specific vibrational modes: E_g for La, A_{1g} for Zr, T_{2g} and E_g for Li, and T_{2g} and A_{1g} for O. These findings strongly support the presence of the pure cubic LLZO phase in SG1. The high intense peaks observed in the 900 - 1100 cm^{-1} range are associated with forming Li_2CO_3 and LiOH . Indeed, it's noteworthy that the Raman bands observed in the cubic LLZO structure, especially in the low-wavenumber region, may result from the presence of static or dynamic disorder related to the highly mobile Li^+ ions. These ions move along isotropic pathways that connect different allowed sites within the cubic LLZO structure. This behavior highlights the complex dynamics of lithium ions

within the material, indicating that their motion and arrangement play a crucial role in the material properties and behavior [25].

In contrast, SG2 displays characteristic peaks at 140, 178, 198, 241, 264, 293, 320, 367, 379, 343, 400, 445, 781, 894, 983, 1018, and 1026 cm^{-1} . These peaks strongly suggest the coexistence of both tetragonal and cubic phases of LLZO in this sample. The presence of these vibrational modes reflects the structural complexity of SG2. The Raman spectrum of SG2 exhibits more spectral characteristics, such as peaks and bands, than the cubic phase. This could be due to the more twisted arrangement of Li^+ ions or the weaker symmetry of the tetragonal garnet-related structure in SG2. In comparison to SG2, the Raman spectra of SG1 show more favorable vibrational modes for cubic LLZO. This shows that when LLZO is exposed to air, a contamination layer emerges, consisting mostly of LiOH and Li_2CO_3 . The intense Raman shift observed in the range of 900 - 1100 cm^{-1} enables the reliable identification of Li_2CO_3 [24].

3.3 Morphology analysis

Figure 4 shows Scanning Electron Microscopic (SEM) images of two samples, SG1 and SG2, which were prepared using a sol-gel process. The SEM micrographs in Figure 4 (a-c) and 5 (e-g) reveal that the microstructure of the calcinated powder (at 1323 K for 12 hours) is heterogeneous. It confirms that both LLZO particles have residual pores present both between particles and within clusters. The SEM images of the SG2 sample, which underwent calcination at 1323 K for 12 hours in a room atmosphere, are depicted in Figure 4 (a-c). The analysis reveals the non-uniform formation of a contamination layer, a combination of $\text{La}_2\text{Zr}_2\text{O}_7$ and Li_2CO_3 . The presence of clusters can be attributed to early melting, possibly of a carbonitic nature, during the heat treatment process, which led to the adhesion of particles.

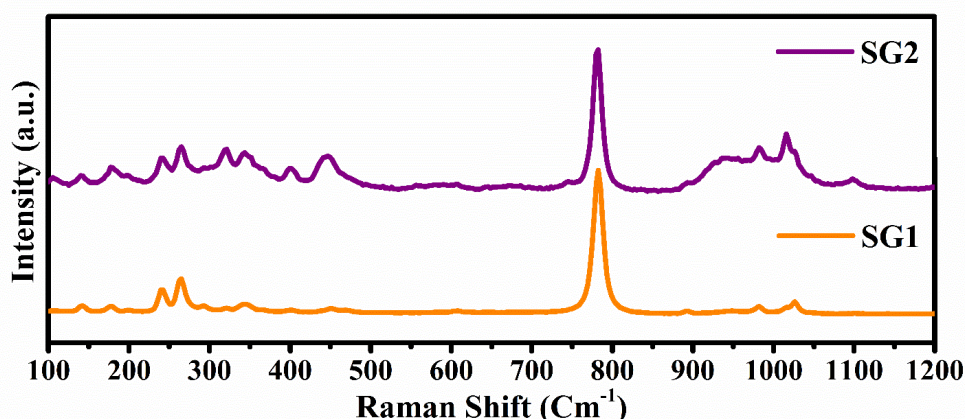


Figure 3. Raman spectra of SG1 and SG2

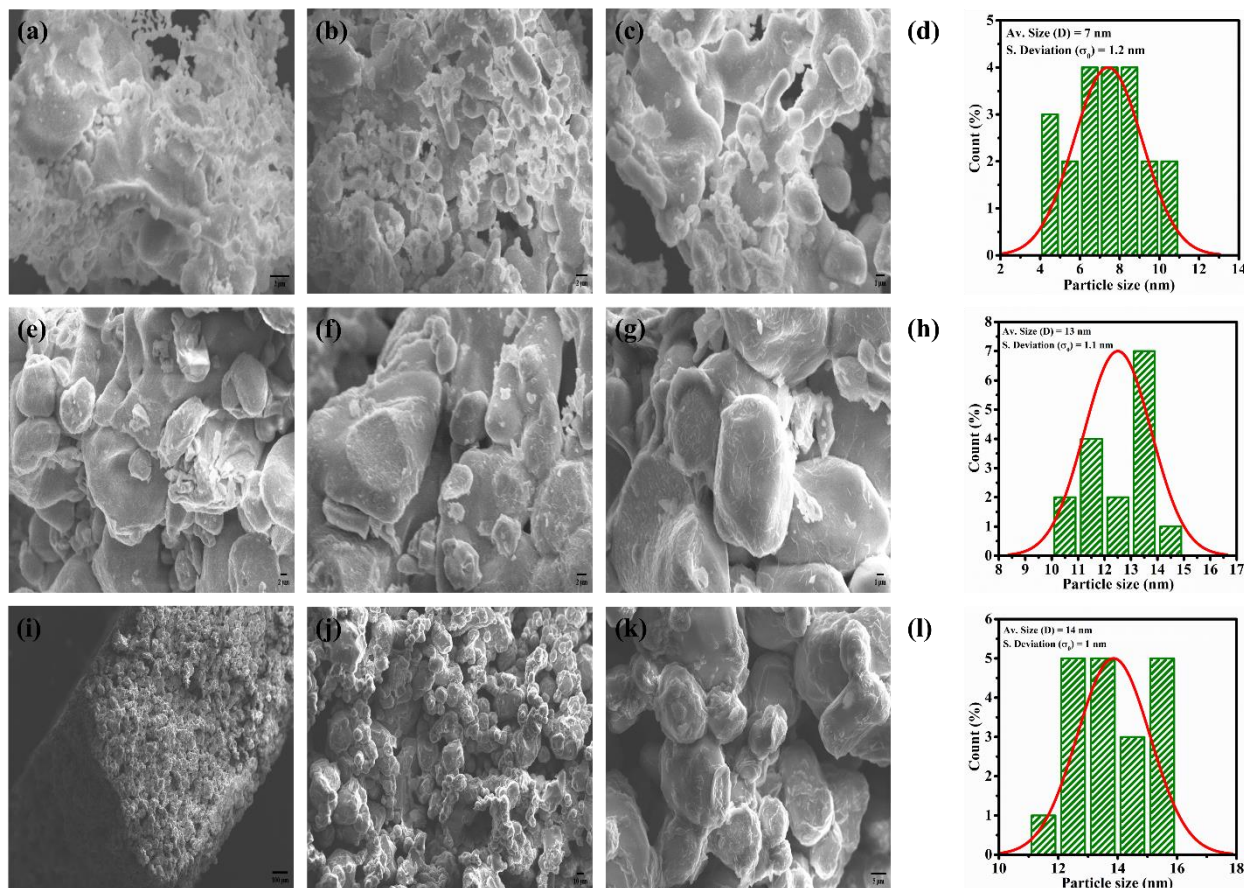


Figure 4. Fig. 4 shows Scanning Electron Microscopic (SEM) images of two samples, SG1 and SG2, which were prepared using a sol-gel process

The particles in Figure 4 (a-c) exhibit irregularly spherical shapes with sizes ranging from 5 to 1 μm . These particles form fine agglomerates. The change of LLZO from the cubic to the tetragonal phase may result in the development of micron-sized agglomerated particles. This transition is anticipated to reduce the ionic conductivity of the bulk material. [21]. Figure 4 (d) depicts the particle size distribution derived from the SEM image in Figure 4 (c). The distribution clarifies that the particles of SG2 have mean particle sizes of 7 nm. The SG2 exhibits a slightly elevated particle distribution.

Figure 4 (e-g, i-k) depict the SEM images of the SG1 sample, which was calcined at 1323 K for 12 hours. The micrograph images in Figure 4 (e-g) depict the cubic LLZO sample SG1, while Figure 4 (i-k) shows the cross-sectional images of the SG1 sample. These images provide insights into the microstructure and morphology of the SG1 sample after the calcination process. The cross-sectional analysis in SG1 is due to the absence of the pyrochlore phase, which typically has a relatively high density and smaller particle size. In Figure 4 (e-g), irregular spherical crystallites are observed, forming large aggregate particles with interparticle pores. At high magnification, uneven particles with holes are visible, suggesting grain breakage during calcination and

indicating a weak grain boundary region. Figure 4 (h) depicts the particle size distribution derived from the SEM image in Figure 4 (g). The distribution clarifies that the particles of SG1 have mean particle sizes of 13 nm. The SG1 exhibits a slightly elevated particle distribution.

Figure 4. Scanning Electron image of SG2 at (a) 2 μm scale, (b) 2 μm scale, and (c) 1 μm scale (d) particle size distribution derived from SG2 sample. Scanning Electron image of SG1 at (e) 2 μm scale (f) 2 μm scale (g) 1 μm scale (h) particle size distribution derived from SG1 sample (i) 100 μm scale (j) 10 μm scale and (k) 5 μm scale (l) particle size distribution derived from SG1 pellet sample.

Figure 4 (i) displays cross-sectional images of SG1, showing the sample's even formation of grains. This even grain growth results in a reduction in the density of grain boundaries. Decreasing the number of grain boundaries and enhancing contact between grains is advantageous for increasing the ionic conductivity of cubic LLZO. Figure 4 (j) and 4 (k) present high-magnification regions of the cross-sectional images at 10 and 5 μm , respectively. The presence of pores within the grains indicates abnormal grain growth. These holes extend into the grains but do not obstruct the path of

lithium diffusion, nor do they create a spatial barrier to lithium-ion conduction. Figure 4 (j) and 4 (k) show that these microstructural alterations are related to an increase in relative density. Furthermore, the lower grain boundary volume ratio and the improved connectivity between larger grains contribute to the reduction in grain boundary resistance [26]. Figure 4 (l) illustrates the particle size distribution derived from the SEM image in Figure 4 (j). The distribution indicates that the size of the SG1 pellet with mean particle sizes of 14 nm. SG1 pellet displays a marginally reduced particle size. Overall, the sample exhibits a consistent particle distribution, irrespective of variations in crystallite sizes. This consistency is attributed to forming the LLZO structure primarily governed by the dispersion mechanism.

3.4 Topographic analysis

Figure 5 (a) and 5 (b) present the two-dimensional (2D) and three-dimensional (3D) topographical images of the SG1 sample pellet. In the 2D topographical image (Figure 5 (a)), it's evident that the grain boundaries appear lower compared to the grain interiors. It shows less uniformity with a high roughness area. This phenomenon indicates a lower Li^+ concentration at the grain boundaries, which can potentially lead to reduced conductivity, making these regions more susceptible to lithium extrusion [27]. Figure 5 (b) illustrates a three-dimensional (3D) image of SG1, covering an area of $4 \mu\text{m} \times 4 \mu\text{m}$. It highlights that the surface of SG1 is characterized by non-uniformly sized particles with variations in height.

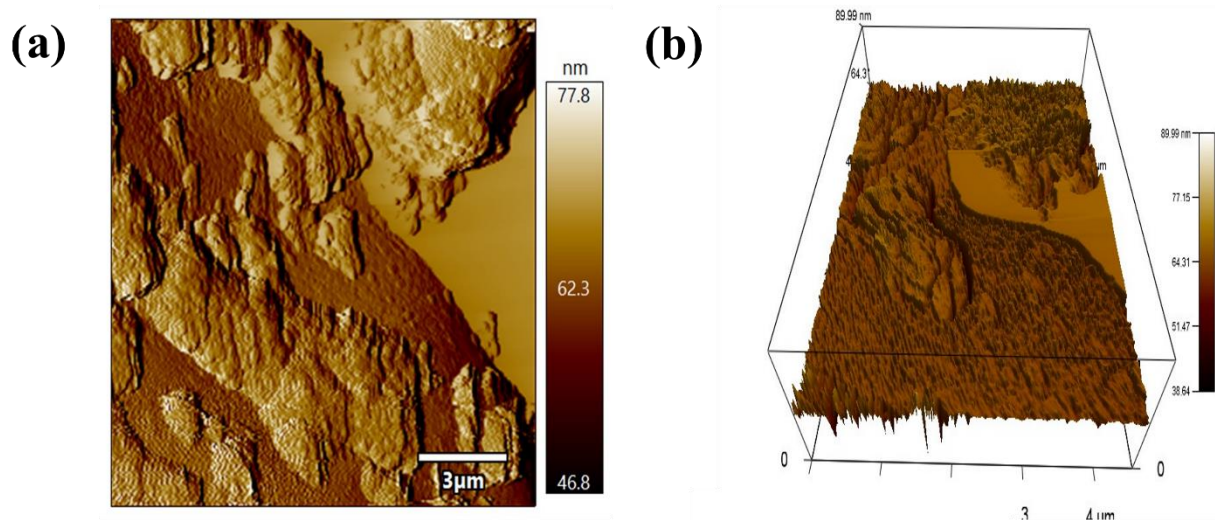


Figure 5. Surface topography of SG1 pellet sample. **(a) & (b)** Two dimensional (2D) and three dimensional (3D) topographical images.

3.5 Conductivity analysis

Figure 6 (a) and 6 (b) depict the impedance spectra of the SG1 and SG2 samples, measured at calcining temperatures of 873 K and 1323 K. Figure 6 (c) and 6 (d) represent the spectra of the SG1 and SG2 samples at 1323 K, measured across temperatures ranging from 323K to 823K. The Nyquist plot observed in the data reveals a distorted semicircular shape at high frequencies and a brief tail at lower frequencies. This distortion is associated with the polarization effect occurring between the electrolyte and the Ag-blocking electrodes. The inset in Figure 6 (c) and 6 (d) provide an enlarged view of the high-frequency spectra.

In Figure 6 (c), SG1 shows lower ionic resistance as the temperature increases, resulting in a smaller semicircle. This reduction in resistance can be attributed to the increased energy gained by ions due to lattice vibration at higher temperatures, making them more conductive compared to room temperature. The observed plots also indicate a short arc, which is a result of the electrode effect. This suggests that the sample is a single-phase cubic material, which aligns with the expected characteristics of purely cubic LLZO [28].

In Figure 6 (d), it is evident that as the temperature increases, all the SG2 curves display a deformed semicircle at high to mid frequencies, along with a tail at low frequencies. This behavior is indicative of the total resistance attributed to LLZO and the ionic blocking electrode, respectively. The observed depression in the mid-frequency regime can be attributed to the presence of twinned tetragonal grains and grain boundaries within the microstructure. This suggests that the sample is not a single-phase cubic material but rather a mixture of cubic and tetragonal phases [19].

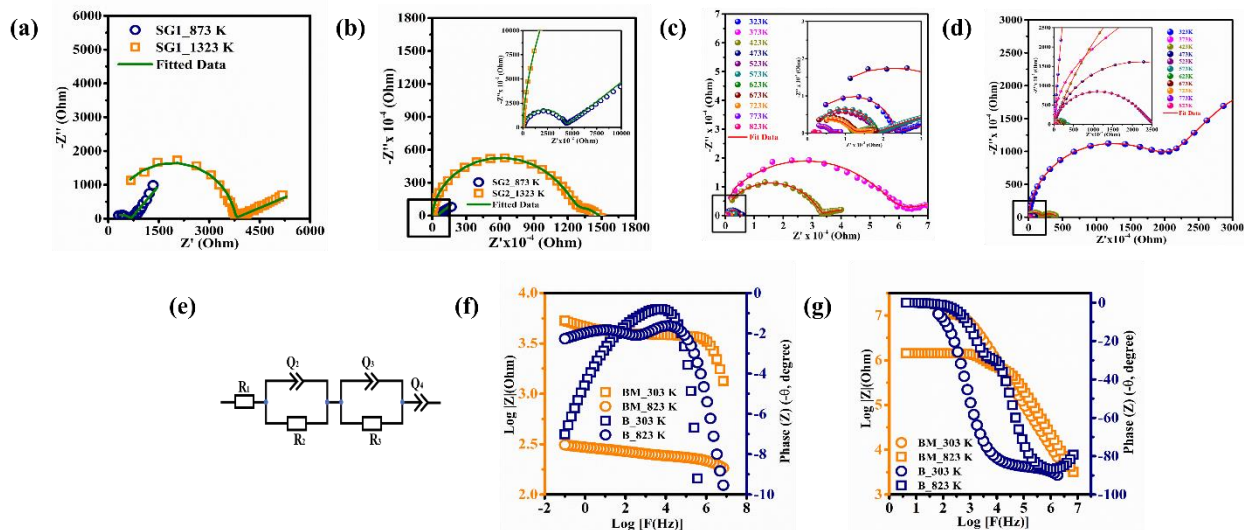


Figure 6. Temperature dependent electrochemical impedance spectroscopy of LLZO SG1 and SG2 samples. (a) and (b) Impedance spectra of SG1 and SG2 at 873 K and 1323 K. (c) and (d) Impedance spectra of SG1 and SG2 at temperatures ranging from 323 K to 823 K. (e) The equivalent circuit diagram used for fitting the impedance spectra. (f) and (g) Bode phase angle and Bode magnitude vs frequency SG1 and SG2 at room temperature (303 K) and 823 K.

Table 1. Impedance parameters calculated from EIS data using the equivalent circuit.

Temperature (In Kelvin)	$\sigma_{SG1} \times 10^{-4}$ S/Cm	$\sigma_{SG2} \times 10^{-4}$ S/Cm
303 K	99.0	69.40
323 K	597.0	-
373 K	10.8	10724.50
423 K	67.6	-
473 K	1.9	1986.77
523 K	1.89	-
573 K	3.56	240.44
623 K	3.78	-
673 K	3.44	34.70
723 K	3.98	-
773 K	5.69	3.33
823 K	0.0014	0.0026

The Bode plots depicted in Figure 6 (f) and 6 (g) play a crucial role in establishing the frequency limits required for extracting electrical parameters through the Complex Non-Linear Least Square fitting function (CNLS). The semicircles observed in the Nyquist plots become more evident in a Bode-type plot (Figure 6 (f) and 6 (g)), namely as minima in the phase shift curve. They are characteristic of R-CPE elements. Based on the information from the Bode plots, an equivalent circuit has been constructed, incorporating RC circuits, as demonstrated in Figure 6 (e). The impedance data was subsequently fitted using the equivalent circuit [R1] [Q2/R2] [Q3], as depicted in Figure 6 (e). In this circuit,

Q3 functions as a blocking double-layer capacitance in series with a parallel combination of grain boundary resistance (R2) and a constant phase element (Q2), while R1 represents the bulk resistance. The ionic conductivity (σ) is calculated using the formula

$$\sigma = l / RS \dots (1)$$

In this equation, R represents resistance, l is the thickness of the sample, and S is the area of the pellet, which can be directly obtained from the apparent ionic conductivity. The calculated values shown in Table 1.

The specific conductivity of calcined SG1 was 2.84×10^{-4} S/cm⁻¹ and 9.90×10^{-5} S/cm⁻¹ at 873 K and

1323 K, determined by intercepting the real axis and considering the sample size. Over the studied temperature range, the highest ionic conductivity, reaching $1.49 \times 10^{-3} \text{ S/cm}^{-1}$, was observed at 823 K. In contrast, the lowest conductivity, which was $1.08 \times 10^{-5} \text{ S/cm}^{-1}$, occurred at 373 K. Similarly, for SG2, the conductivity at 873 K and 1323 K was calculated as $4.55 \times 10^{-7} \text{ S/cm}^{-1}$ and $6.94 \times 10^{-8} \text{ S/cm}^{-1}$. Across the temperature range, the highest ionic conductivity recorded was $2.63 \times 10^{-3} \text{ S/cm}^{-1}$ at 823 K, with the lowest conductivity being $1.07 \times 10^{-5} \text{ S/cm}^{-1}$ at 373 K. This indicates that there are variations in conductivity for the samples at different temperatures, with SG1 consistently displaying higher conductivity than SG2 across the entire temperature range.

The Bode graphs in Figure 6(f) and 6(g) show the connection between frequency, phase, and magnitude of impedance modulus (Z) for SG1 and SG2 samples at 303 and 823 K, respectively. The Bode phase plot of the 303 K spectra for SG1 shows a high-frequency region in which ions in the space charge layer contribute to changes in grain and grain border resistance. In contrast, behaviours found in the intermediate to low-frequency domain are controlled by ion dynamics, particularly at grain boundaries. At 823 K, the Bode phase plot is associated with the response of the interfacial region between the Solid Electrolyte (SE) and the blocking electrode on the SE, indicating different ion dynamics compared to the lower temperature. Meanwhile, the SG2 sample exhibits two superimposed semicircles, which are also observed in the Nyquist plots, representing ion movement in the grain and grain boundary regions in the presence of a blocking electrode. This suggests more complex ion dynamics in SG2.

On the other hand, the Bode magnitude plot of SG1 and SG2 (showing impedance modulus Z as a function of frequency) emphasizes a significant impact from grain boundary resistance in the mid to lower-frequency range. However, at higher frequencies, the grain's contribution to the total impedance surpasses that of the grain boundary. Therefore, the intricate behavior of the Solid Electrolyte (SE) stems from the interplay of various processes occurring in both the grain and grain boundary regions.

Arrhenius relation

Figure 7 (a) and 7 (b) depict the Arrhenius plots of bulk conductivity (σ) based on the data from Figure 6 (c) and 6 (d). The activation energy (E_a) was calculated using the slope of the $\log(\sigma T)$ versus the $1000/T$ plot. The Arrhenius equation (Equation 2) was employed to linearly fit and determine the activation energy (E_a) for the overall ionic conductivity. The Arrhenius equation is expressed as

$$\sigma T = A \exp(E_a / k_B T) \quad \dots (2)$$

where A represents the pre-exponential parameter, k_B is Boltzmann's constant, and T is the absolute temperature. The activation energy (E_a) values for SG1 and SG2 were determined to be around 0.37 eV and 0.68 eV, respectively, over a temperature range spanning from 373K to 823K. Notably, SG1 exhibits higher Li^+ ion mobility at elevated temperatures. The fact that SG1 demonstrates a low activation energy of 0.37 eV is a noteworthy characteristic, which renders LLZO a promising choice for efficient ion conduction and energy storage applications.

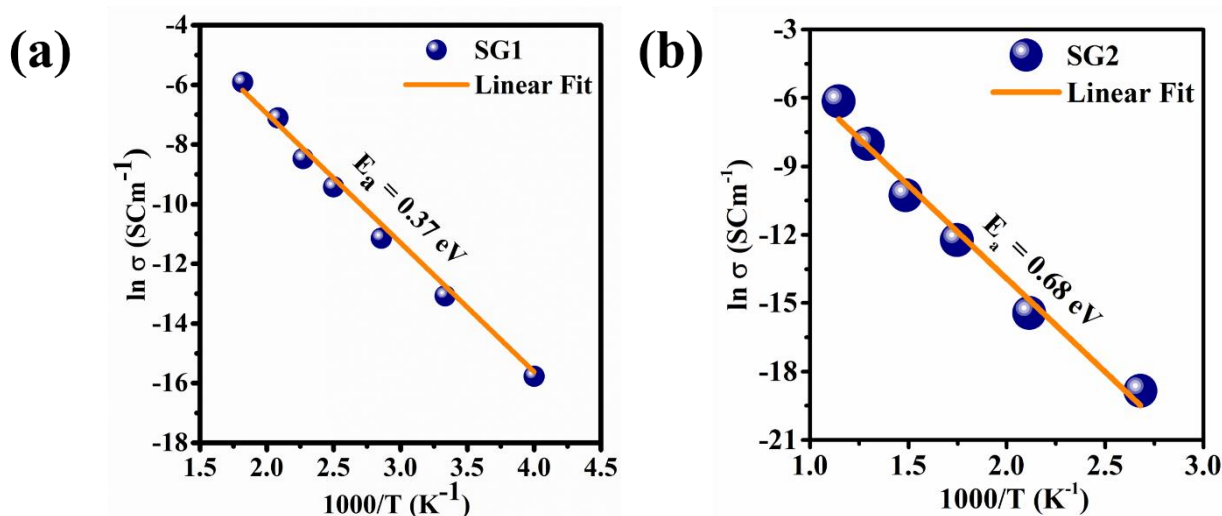


Figure 7. A linear correlated plot of ionic conductivity vs temperature of SG1 and SG2.

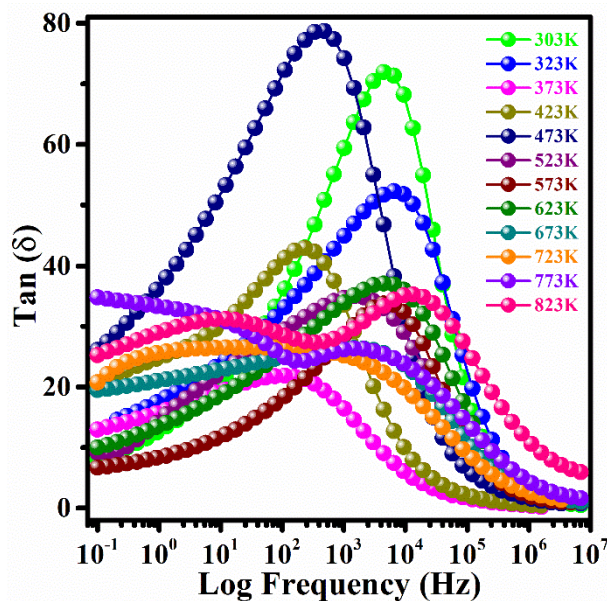


Figure 8. Dielectric loss tangent ($\tan \delta$) of SG-1 pellet was measured over a temperature range from 303K to 823K.

3.6 Dielectric analysis

The loss (δ) tangent is studied to understand the relaxation process during conduction. It is defined as the ratio of the real and imaginary parts of permittivity.

$$\tan \delta = \epsilon''/\epsilon' \tag{3}$$

The values of ϵ' and ϵ'' were calculated using the below equation.

$$\epsilon' = \frac{Z''}{\omega C_0(Z'^2 + Z''^2)} \text{ and } \epsilon'' = \frac{Z'}{\omega C_0(Z'^2 + Z''^2)} \tag{4}$$

where, C_0 is the capacitance of electrode ($C_0 = \epsilon_0 \frac{A}{d}$; $\epsilon_0 = 8.85 \times 10^{-12} \text{ F/m}$ is the permittivity of free space), d and A are the thickness and area of electrolyte, Z' and Z'' is real and imaginary part of complex impedance. ω is the angular frequency ($\omega = 2\pi f$), where f is the frequency of the applied electric field.

The $\tan \delta$ plot in Figure 8 illustrates the relaxation peak associated with bulk ionic transport at various temperatures, ranging from 303K to 823K, for the SG-1 pellet under investigation. The loss spectrum is attributed to space charge and dipolar polarization at both lower and higher frequencies. As the temperature increases, the relaxation peaks observed in the low-frequency region consistently shift towards higher frequencies. This shift indicates a shorter relaxation time, reflecting a more rapid ionic migration between adjacent sites and a short segmental relaxation of charge carriers. Notably, temperature ranges between 673K and 823K exhibit double distinct relaxation peaks, one in the low-frequency region and another in the high-frequency region. These double relaxation peaks suggest ionic transport in bulk and grain boundary regions. The lower intensity of the peaks indicates

smaller dielectric loss in the material, implying enhanced conduction properties [29].

3.7 Electric Modulus

Complex electrical modulus formalism is an important tool for understanding charge-transport processes. Through the following equation, the complex electric modulus (M^*) can be calculated from the complex impedance (Z),

$$M^* = M' + i M'' = i\omega C_0(Z' + Z'') \tag{5}$$

The real and imaginary parts can be separated as $M' = \omega C_0 Z'$ and $M'' = -\omega C_0 Z''$. Figure 10 represents the complex electric modulus spectra, including both the real and imaginary parts, for the SG-1 pellet. The measurements were conducted at various temperatures, ranging from 303K to 823K.

In Figure 9 (a), the real modulus (M') exhibits its lowest values at lower frequencies, primarily due to electrode effects associated with the suppressed modulus method. However, at higher frequencies, M' remains more stable, indicating a frequency-independent behavior. This stability arises from the absence of interfacial polarization caused by material inhomogeneity. Figure 9 (b) shows the imaginary modulus (M''), which displays frequency-independent behavior in the lower frequency region. This behavior is linked to the long-range migration of Li^+ ions, involving hopping from one site to another. It suggests that the peak observed in the modulus spectrum is a result of the conductivity relaxation associated with the mobility of Li^+ ions. Notably, there is no relaxation behavior in ionic conductivity, but rather, a re-orientation of lithium ions occurs at octahedral sites (48 g to 96 h) when a relaxation peak appears on the higher frequency side.

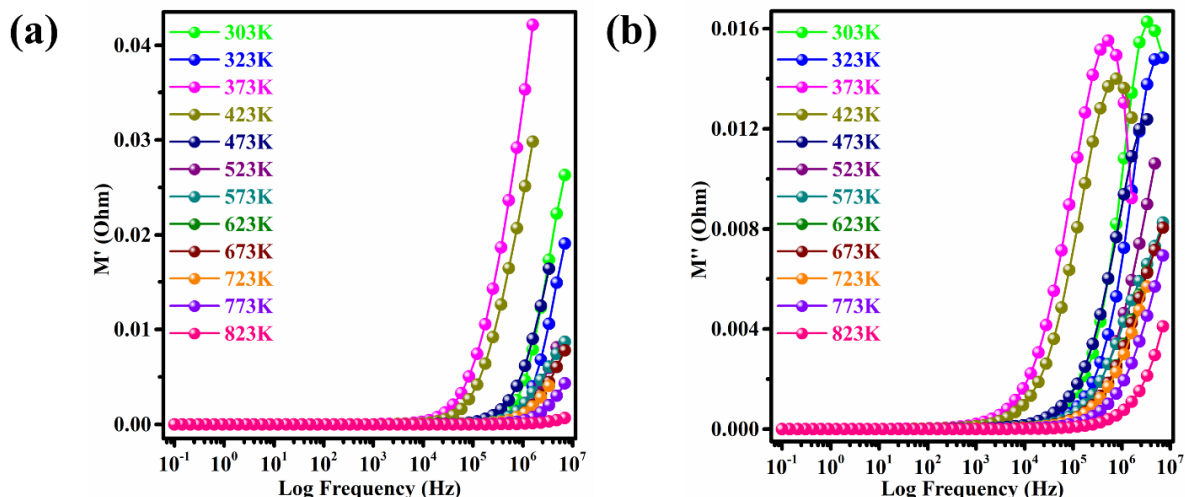


Figure 9. Electric modulus (a) real M' (b) imaginary M'' of SG-1 were measured over a temperature range from 303K to 823K.

Table 2. Calculated power density (P) and energy density (E) of the fabricated device from the charge-discharge analysis

Current (mA)	Energy density (Wh/kg)	Power density (W/kg)
0.5	1.95	144.92
0.6	1.20	173.91
0.7	0.69	201.89
0.8	0.40	245.88
0.9	0.22	301.86
1	0.14	351.85
1.5	0.07	434.78
2	0.02	579.71

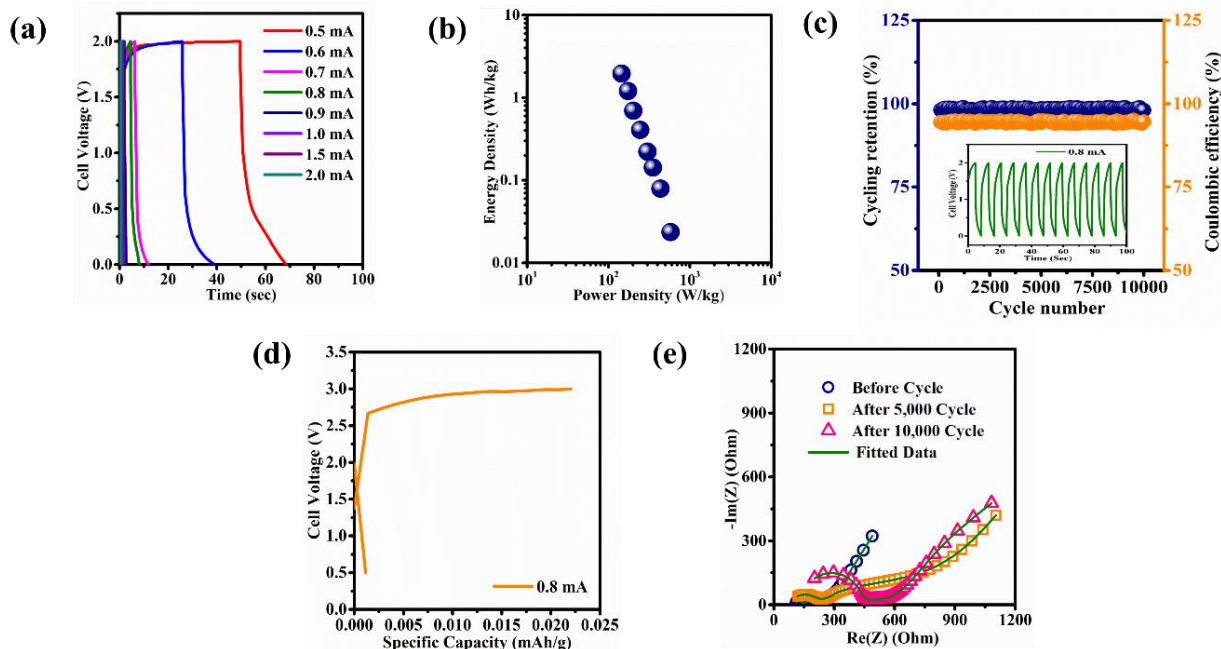


Figure 10 shows the electrochemical performance of the $\text{LiFePO}_4/\text{LLZO}/\text{AC}$ device. (a) Charge/discharge profiles at various rates (0.5-2 mA). (b) Rangone plot labeled for current density. (c) Coulombic efficiency and cycling retention at 0.8 mA (cycling performance is displayed in the inset of the figure). (d) A charge/discharge arc with 1mA voltages varying from 0.5 to 3 V. (e) A Nyquist plot showing before and after 10,000 cycles.

Table 3. Performance evaluation of LLZO ceramic solid electrolyte with other related works.

Electrolyte Composition Li ₇ La ₃ Zr ₂ O ₁₂ (LLZO)	Materials		SSD Configuration	Electrolyte Preparation for SSD	σ (SCm ⁻¹) at (303 K)	Cyclic Retention/ Number	Cell Voltage/ Assembled	Ref.
	Method	Anode/ Cathode						
LLZO Nanoparticle	Sol-Gel	Li/LiFePO ₄ (LFP)	Li/PLL/LFP	Polymer Electrolyte	3.02 × 10 ⁻⁵	93.5% / 200 Cycles	3.0 -6.0 V/ Glove box	[21]
Li ₇ La ₃ Zr ₂ O ₁₂	Solid- State Reaction	Li/LiFePO ₄ (LFP)	Li/LLZO/LFPO	solid state battery	2.4 × 10 ⁻³	99%/ 100 Cycles	-0.3 -5.0 V/ Glove box	[23]
LLZO Nano fiber	Tape casting process	Li/ (S/NC)	Li/LLZO/(S/NC)	Polymer composites	-	100 Cycles	2.6 - 4.3 V/ Glove box	[27]
Li _{6.61} La ₃ Zr ₂ Al _{0.13} O _{11.98} Nanoparticles	Solid- State Route	Li/LiCoO ₂ (LCO)	Li/ (1 M LiPF ₆ + LLZO)/LCO	Hybrid cell	1.95 × 10 ⁻¹¹	92.7% / 50 Cycles	3.0 - 4.2 V / RT	[31]
Li _x La ₃ Zr ₂ O ₁₂	Sol-gel	Li/LiCoO ₂ (LCO)	Li/ LLZO/LCO	solid state battery	1.02×10 ⁻⁴	-	3.0-3.9 V/ Glove box	[32]
Li ₇ La ₃ Zr ₂ O ₁₂ Fillers	-	NCM622/Li	NCM622/CSE/Li	Composites solid electrolyte	1.75×10 ⁻⁴	100 Cycles	2.0 -4.2 V/ Glove box	[33]
Li ₇ La ₃ Nb ₂ O ₁₂	Ball-milling process	Li ⁺ /Li ⁻	Li ⁺ /LLZO/Li ⁻	solid state battery	-	45 Cycles	2.5 -4.2 V/ Glove box	[34]
Li ₇ La ₃ Zr ₂ O ₁₂	Sol-gel	AC/LiFePO ₄	LFP/LLZO/AC	Solid electrolyte	2.08 × 10 ⁻⁴	93%/ 10,000 Cycles	2.0- 4.0V/ RT	This Work

The shift in the peak position toward higher frequencies suggests that Li-ion re-orientation is thermally initiated. As temperatures increase from 323K to 423K, a prominent peak emerges due to the re-orientation of Li⁺ ions as they transition between octahedra around the immobile tetrahedral site. In the temperature range of 473K to 823K, the shift in peak position towards higher frequencies tends to decrease, indicating the prevalence of long-range migration for Li⁺ ions instead of short-range re-orientation [30].

3.8 Electrochemical performance of LiFePO₄/LLZO/AC device

An SSD (solid-state device) LiFePO₄/LLZO/AC has been developed exhibits an initial impedance of 150 Ohms (as observed in Figure 10 (e)). This suggests that the developed solid-state electrolyte (SSE) device makes good interfacial contact with the current collector and electrolytes. Figure 10 (a) depicts the charge/discharge profile of the LiFePO₄/LLZO/AC device at different current densities, ranging from 0.5 to 2 mA at 303 K [19]. The values of energy density (E), and power density (P) was calculated using the formula described in Agnes et.al [19]. The calculated values were shown in Table 2.

The Ragone plot in Figure 10 (b) depicts the LiFePO₄/LLZO/AC device's performance for energy storage applications. The device operates at 2V, has an energy density of 1.95 Wh/kg, and a power density of 144.92 W/kg at a current density of 0.5 mA. In addition, the LiFePO₄/LLZO/AC device was charged and discharged 10,000 times at 100 mV/s for 2 mA. Figure 10 (c) shows the associated cyclic retention and Coulombic efficiency evolution.

An inset in Figure 10 (c) shows a part of the charge/discharge curve, confirming the device's stable and consistent performance. Throughout the 10,000

cycles, the Coulombic efficiency remained at around 93%. Cyclic capacitance retention showed a variable tendency, ranging from 85.4% to 90.7%, with an average of 86%. Even after 10,000 cycles, the charge/discharge curves remain quasi-triangular, suggesting the device's high specific capacitance retention. Figure 10 (d) illustrates the charge/discharge arc of 1 mA, ranging from 0.5 to 3 V. The variation in voltage has been analyzed to assess whether the material exhibits the capability to operate above 2V. Upon analysis, the obtained energy density value is 0.75 Wh/kg for a 0.8 mA current.

Figure 10 (e) shows the Nyquist plot of the LiFePO₄/LLZO/AC device before and during cycling at 303 K. The data recorded before cycling (at 303 K) shows two depressed semicircles in the high to mid-frequency range, showing charge transfer resistance at the electrode-electrolyte interface, and an angled line in the low-frequency zone, representing Warburg impedance. The Warburg impedance is related to the passage of Li⁺ ions from the electrode to the electrolyte. Changes in resistance become evident after 5,000 cycles. At 5,000 and 10,000 cycles, the recorded semicircles transform into semi-arcs in the high-frequency region, indicating that charge transfer becomes more prominent in the initial cycling stages. The mid-frequency region represents the interface formed between the electrode and electrolyte, with an inclined slope observed in the low-frequency range. After completing 10,000 cycles, the resistance associated with charge transfer appears to be lower than it was at 5,000 cycles, suggesting an acceleration in kinetics brought about by electrochemical activation. A comparative analysis of the observed cell conduction behavior with data from Table 3 underscores the outstanding cyclic stability of the solid-state device at room temperature, rendering it highly promising for practical energy storage applications with high energy densities.

4. Conclusion

The dissociation behavior of water-soluble salts of Li and La, along with the distinct behavior of Zr sources, results in the generation of Li^+ and La^{3+} ions and Zr^{4+} ions in aqueous solutions. The specific conductivity of calcined SG1 and SG2 exhibits temperature-dependent variations, with SG1 consistently displaying higher conductivity across the temperature range. The controllable mass transfer of lithium, facilitated by the closed-packed structure, enhances ionic conductivity. The $\text{LiFePO}_4/\text{LLZO}/\text{AC}$ device, constructed using these electrolytes, demonstrates an impressive energy density of 1.95 Wh/kg and a power density of 144.92 W/kg, showcasing excellent solid electrode-electrolyte interphase. The cyclic stability over 10,000 cycles, with an average performance of 86%, underscores the potential of LLZO as a solid electrolyte for advanced energy storage devices. The sol-gel synthesis and densification strategy is a simple and effective method for obtaining lithium-rich LLZO electrolytes. The enhanced ionic conductivity and electrochemical performance of the solid-state device emphasize the practical viability of this approach, contributing to the sustainable development of advanced energy storage technologies.

References

- [1] S.R. Yeandel, B.J. Chapman, P.R. Slater, P. Goddard, Structure and lithium-ion dynamics in fluoride-doped cubic $\text{Li}_7\text{La}_3\text{Zr}_2\text{O}_{12}$ (LLZO) garnet for Li solid-state battery applications. *Journal of Physical Chemistry C*, 122(49), (2018) 27811-27819. <https://doi.org/10.1021/acs.jpcc.8b07704>
- [2] S. Smetaczek, E. Pycha, J. Ring, M. Siebenhofer, S. Ganschow, S. Berendts, A. Nanning, M. Kubicek, D. Rettenwander, A. Limbeck, Investigating the electrochemical stability of $\text{Li}_7\text{La}_3\text{Zr}_2\text{O}_{12}$ solid electrolytes using field stress experiments, *Journal of Materials Chemistry A*, 9(27), (2021) 15226-15237. <https://doi.org/10.1039/D1TA02983E>
- [3] S. Yu, R.D. Schmidt, R. Garcia-Mendez, E. Herbert, N.J. Dudney, J.B. Wolfenstine, J. Sakamoto, D.J. Siegel, Elastic properties of the solid electrolyte $\text{Li}_7\text{La}_3\text{Zr}_2\text{O}_{12}$ (LLZO). *Chemistry of Materials*, 28(1), (2016) 197-206. <https://doi.org/10.1021/acs.chemmater.5b03854>
- [4] P.G. Bruce, A.R. West, Phase diagram of the LISICON, solid electrolyte system, $\text{Li}_4\text{GeO}_4\text{-Zn}_2\text{GeO}_4$. *Materials Research Bulletin*, 15(3), (1980) 379-385. [https://doi.org/10.1016/0025-5408\(80\)90182-8](https://doi.org/10.1016/0025-5408(80)90182-8)
- [5] M. Murayama, R. Kanno, M. Irie, S. Ito, T. Hata, N. Sonoyama, Y. Kawamoto, Synthesis of new lithium ionic conductor thio-LISICON-lithium silicon sulfides system. *Journal of Solid State Chemistry*, 168(1), (2002) 140-148. <https://doi.org/10.1006/jssc.2002.9701>
- [6] M. Hou, F. Liang, K. Chen, Y. Dai, D. Xue, Challenges and perspectives of NASICON-type solid electrolytes for all-solid-state lithium batteries. *Nanotechnology*, 31(13), (2020) 132003. <https://doi.org/10.1088/1361-6528/ab5be7>
- [7] R. DeWees, H. Wang, Synthesis and properties of NaSICON-type LATP and LAGP solid electrolytes. *ChemSusChem*, 12(16), (2019) 3713-3725. <https://doi.org/10.1002/cssc.201900725>
- [8] M. Catti, First-principles modeling of lithium ordering in the LLTO ($\text{Li}_x\text{La}_{2/3-x}\text{TiO}_3$) superionic conductor. *Chemistry of Materials*, 19(16), (2007) 3963-3972. <https://doi.org/10.1021/cm0709469>
- [9] C. Uhlmann, P. Braun, J. Illig, A. Weber, E. Ivers-Tiffée, Interface and grain boundary resistance of a lithium lanthanum titanate ($\text{Li}_3\text{La}_2/3\text{-xTiO}_3$, LLTO) solid electrolyte. *Journal of Power Sources*, 307, (2016) 578-586. <https://doi.org/10.1016/j.jpowsour.2016.01.002>
- [10] S. Cao, S. Song, X. Xiang, Q. Hu, C. Zhang, Z. Xia, Y. Xu, W. Zha, J. Li, P.M. Gonzalez, Y-H. Han, F. Chen, Modeling, preparation, and elemental doping of $\text{Li}_7\text{La}_3\text{Zr}_2\text{O}_{12}$ garnet-type solid electrolytes: A review. *Journal of the Korean Ceramic Society*, 56(2), (2019) 111-129. <https://doi.org/10.4191/kcers.2019.56.2.01>
- [11] D. Mazza, Remarks on a ternary phase in the $\text{La}_2\text{O}_3\text{-Me}_2\text{O}_5\text{-Li}_2\text{O}$ system (Me=Nb, Ta). *Materials Letters*, 7(5-6), (1988) 205-207. [https://doi.org/10.1016/0167-577X\(88\)90011-0](https://doi.org/10.1016/0167-577X(88)90011-0)
- [12] H. Hyooma, K. Hayashi, Crystal structures of $\text{La}_3\text{Li}_5\text{M}_2\text{O}_{12}$ (M=Nb, Ta). *Materials Research Bulletin*, 23(10), (1988) 1399-1407. [https://doi.org/10.1016/0025-5408\(88\)90264-4](https://doi.org/10.1016/0025-5408(88)90264-4)
- [13] V. Thangadurai, H. Kaack, W.J.F. Weppner, Novel fast lithium ion conduction in garnet-type $\text{Li}_5\text{La}_3\text{M}_2\text{O}_{12}$ (M= Nb, Ta). *Journal of the American Ceramic Society*, 86(3), (2003) 437-440. <https://doi.org/10.1111/j.1151-2916.2003.tb03318.x>
- [14] R. Murugan, V. Thangadurai, W. Weppner, Fast lithium ion conduction in garnet-type $\text{Li}_7\text{La}_3\text{Zr}_2\text{O}_{12}$. *Angewandte Chemie International Edition*, 46(41), (2007) 7778-7781. <https://doi.org/10.1002/anie.200701144>

- [15] J. Awaka, N. Kijima, H. Hayakawa, J. Akimoto, Synthesis and structure analysis of tetragonal $\text{Li}_7\text{La}_3\text{Zr}_2\text{O}_{12}$ with the garnet-related type structure. *Journal of Solid State Chemistry*, 182(8) (2009) 2046-2052. <https://doi.org/10.1016/j.jssc.2009.05.020>
- [16] J. Awaka, A. Takashima, K. Kataoka, N. Kijima, Y. Idemoto, J. Akimoto, Crystal structure of fast lithium-ion-conducting cubic $\text{Li}_7\text{La}_3\text{Zr}_2\text{O}_{12}$, *Chemistry Letters*, 40(1), (2011) 60-62. <https://doi.org/10.1246/cl.2011.60>
- [17] K.B. Dermenci, S. Turan, Structural insights on understanding the cubic phase stabilization mechanism of sol-gel synthesized $\text{Li}_{7-3x}\text{Al}_x\text{La}_3\text{Zr}_2\text{O}_{12}$ ($x=0-0.4$)-The effect of ZrOCl_2 and $\text{ZrO}(\text{NO}_3)_2$, *Ceramics International*, 44(10), (2018) 11852-11857. <https://doi.org/10.1016/j.ceramint.2018.03.277>
- [18] I. Kokal, M. Somer, P.H.L. Notten, H.T. Hintzen, Sol-gel synthesis and lithium ion conductivity of $\text{Li}_7\text{La}_3\text{Zr}_2\text{O}_{12}$ with garnet-related type structure, *Solid State Ionics*, 185(1), (2011) 42-46. <https://doi.org/10.1016/j.ssi.2011.01.002>
- [19] A. Lakshmanan, R. Gurusamy, S. Venkatachalam, Enhanced total ionic conductivity of NASICON-type solid-state electrolyte $\text{Li}_{1+x}\text{Al}_x\text{Ti}_{2-x}(\text{PO}_4)_3$. *Ionics*, 29(12), (2023) 5123-5138. <https://doi.org/10.1007/s11581-023-05222-5>
- [20] Y. Tian, Y. Zhou, Y. Liu, C. Zhao, W. Wang, Y. Zhou, Formation mechanism of sol-gel synthesized $\text{Li}_{7-3x}\text{Al}_x\text{La}_3\text{Zr}_2\text{O}_{12}$ and the influence of abnormal grain growth on ionic conductivity. *Solid State Ionics*, 354, (2020) 115407. <https://doi.org/10.1016/j.ssi.2020.115407>
- [21] Q.H. Nguyen, V.T. Luu, H.L. Nguyen, Y.-W. Lee, Y. Cho, S.Y. Kim, Y.-S. Jun, W. Ahn, $\text{Li}_7\text{La}_3\text{Zr}_2\text{O}_{12}$ garnet solid polymer electrolyte for highly stable all-solid-state batteries. *Frontiers in Chemistry*, 8, (2021) 619832. <https://doi.org/10.3389/fchem.2020.619832>
- [22] Y. Zhang, W. Luo, D. Hu, Y. Deng, Y. Chen, J. Deng, Rapid Fabrication of $\text{Li}_7\text{La}_3\text{Zr}_2\text{O}_{12}$ Solid Electrolyte with Enhanced Lithium Ionic Conductivity by Microwave Sintering. *International Journal of Electrochemical Science*, 15(8), (2020) 7163-7174. <https://doi.org/10.20964/2020.08.67>
- [23] T. Yang, J. Zheng, Q. Cheng, Y.-Y. Hu, C.K. Chan, Composite polymer electrolytes with $\text{Li}_7\text{La}_3\text{Zr}_2\text{O}_{12}$ garnet-type nanowires as ceramic fillers: mechanism of conductivity enhancement and role of doping and morphology, *ACS applied materials & interfaces*, 9(26), (2017) 21773-21780. <https://doi.org/10.1021/acsami.7b03806>
- [24] A. Sharafi, S. Yu, M. Naguib, M. Lee, C. Ma, H.M. Meyer, J. Nanda, M. Chi, D.J. Siegel, J. Sakamoto, Impact of air exposure and surface chemistry on $\text{Li}-\text{Li}_7\text{La}_3\text{Zr}_2\text{O}_{12}$ interfacial resistance, *Journal of Materials Chemistry A*, 5(26), (2017) 13475-13487. <https://doi.org/10.1039/C7TA03162A>
- [25] F. Tietz, T. Wegener, M.T. Gerhards, M. Giarola, G. Mariotto, Synthesis and Raman micro-spectroscopy investigation of $\text{Li}_7\text{La}_3\text{Zr}_2\text{O}_{12}$, *Solid State Ionics*, 230, (2013) 77-82. <https://doi.org/10.1016/j.ssi.2012.10.021>
- [26] Z. Cao, W. Wu, Y. Li, J. Zhao, W. He, J. Liu, H. Zhang, G. Li, Lithium ionic conductivity of $\text{Li}_{7-3x}\text{FexLa}_3\text{Zr}_2\text{O}_{12}$ ceramics by the Pechini method. *Ionics*, 26 (2020) 4247-4256. <https://doi.org/10.1007/s11581-020-03580-y>
- [27] Z. Lu, Z. Yang, C. Li, K. Wang, J. Han, P. Tong, G. Li, B.S. Vishnugopi, P.P. Mukherjee, C. Yang, W. Li, Modulating Nanoinhomogeneity at Electrode–Solid Electrolyte Interfaces for Dendrite-Proof Solid-State Batteries and Long-Life Memristors. *Advanced Energy Materials*, 11(16), (2021) 2003811. <https://doi.org/10.1002/aenm.202003811>
- [28] W. Lan, H. Fan, V.W.-h. Lau, J. Zhang, J. Zhang, R. Zhao, H. Chen, Realizing $\text{Li}_7\text{La}_3\text{Zr}_2\text{O}_{12}$ garnets with high Li^+ conductivity and dense microstructures by Ga/Nb dual substitution for lithium solid-state battery applications, *Sustainable Energy & Fuels*, 4(4), (2020) 1812-1821. <https://doi.org/10.1039/C9SE01162E>
- [29] D.M. Abdel-Basset, S. Mulmi, M.S. El-Bana, S.S. Fouad, V. Thangadurai, Structure, Ionic Conductivity, and Dielectric Properties of Li-Rich Garnet-type $\text{Li}_{5+2x}\text{La}_3\text{Ta}_2-x\text{Sm}_x\text{O}_{12}$ ($0 \leq x \leq 0.55$) and Their Chemical Stability. *Inorganic chemistry*, 56(15), (2017) 8865-8877. <https://doi.org/10.1021/acs.inorgchem.7b00816>
- [30] J.-F. Wu, E.-Y. Chen, Y. Yu, L. Liu, Y. Wu, W.K. Pang, V.K. Peterson, X. Guo, Gallium-doped $\text{Li}_7\text{La}_3\text{Zr}_2\text{O}_{12}$ garnet-type electrolytes with high lithium-ion conductivity, *ACS Applied Materials & Interfaces*, 9(2), (2017) 1542-1552. <https://doi.org/10.1021/acsami.6b13902>
- [31] P.J. Kumar, K. Nishimura, M. Senna, A. Düvel, P. Heitjans, T. Kawaguchi, N. Sakamoto, N. Wakiya, H. Suzuki, A novel low-temperature solid-state route for nanostructured cubic garnet $\text{Li}_7\text{La}_3\text{Zr}_2\text{O}_{12}$ and its application to Li-ion battery. *RSC Advances*, 6(67), (2016) 62656-62667. <https://doi.org/10.1039/C6RA09695F>
- [32] G.H. Kim, M.J. Kim, H.B. Kim, J.H. Ryu, H.C. Lee, Preparation and Characterization of Sol-Gel-Driven $\text{Li}_x\text{La}_3\text{Zr}_2\text{O}_{12}$ Solid Electrolytes and

LiCoO₂ Cathodes for All-Solid-State Lithium-Ion Batteries. *Journal of Nanoscience and Nanotechnology*, 20(11), (2020) 7002-7009. <https://doi.org/10.1166/jnn.2020.18838>

- [33] F. Chen, M.X. Jing, H. Yang, W.Y. Yuan, M.Q. Liu, Y.S. Ji, S. Hussain, X.Q. Shen, Improved ionic conductivity and Li dendrite suppression of PVDF-based solid electrolyte membrane by LLZO incorporation and mechanical reinforcement. *Ionics*, 27 (2021) 1101-1111. <https://doi.org/10.1007/s11581-020-03891-0>
- [34] X. Yan, Z. Li, H. Ying, F. Nie, L. Xue, Z. Wen, W.-Q. Han, A novel thin solid electrolyte film and its application in all-solid-state battery at room temperature. *Ionics*, 24 (2018) 1545-1551. <https://doi.org/10.1007/s11581-017-2353-x>

Acknowledgement

The author, Agnes Lakshmanan, is grateful to the Shiksha Abhiyan (RUSA), Government of India, for providing the characterization facilities at the Department of Renewable Energy Science, Manonmaniam Sundaranar University, Tirunelveli, Tamil Nadu, India.

Author's contribution

All authors contributed to the study's conception and design. Agnes Lakshmanan performed material preparation, data collection, analysis, conductivity measurements and dielectric investigations. Sabarinathan Venkatachalam contributed to the manuscript conceptualization, supervision, and editing. Both the authors read and approved the final version of the manuscript.

Has this article screened for similarity?

Yes

Conflict of Interest

The authors declare that they have no conflict of interest.

About the License

© The Author(s) 2024. The text of this article is open access and licensed under a Creative Commons Attribution 4.0 International License.